Available online at www.sciencedirect.com
SCIENCE DIRECT®
Journal of Solid State Chemistry 175 (2003) 94–109
JOURNAL OF SOLID STATE CHEMISTRY
http://elsevier.com/locate/jssc

Investigations of the electronic structure of d^0 transition metal oxides belonging to the perovskite family

Hank W. Eng, Paris W. Barnes, Benjamin M. Auer, and Patrick M. Woodward*

Department of Chemistry, The Ohio State University, 100 W. 18th Ave, Columbus, OH 43210, USA

Received 5 February 2003; received in revised form 1 May 2003; accepted 12 May 2003

Abstract

Computational and experimental studies using linear muffin tin orbital methods and UV-visible diffuse reflectance spectroscopy, respectively, were performed to quantitatively probe the relationships between composition, crystal structure and the electronic structure of oxides containing octahedrally coordinated d^0 transition metal ions. The ions investigated in this study (Ti^{4+}, Nb^{5+}, Ta^{5+}, Mo^{6+}, and W^{6+}) were examined primarily in perovskite and perovskite-related structures. In these compounds the top of the valence band is primarily oxygen $2p$ non-bonding in character, while the conduction band arises from the π^* interaction between the transition metal t_{2g} orbitals and oxygen. For isostructural compounds the band gap increases as the effective electronegativity of the transition metal ion decreases. The effective electronegativity decreases in the following order: $Mo^{6+} > W^{6+} > Nb^{5+} \sim Ti^{4+} > Ta^{5+}$. The band gap is also sensitive to changes in the conduction band width, which is maximized for structures possessing linear M–O–M bonds, such as the cubic perovskite structure. As this bond angle decreases (e.g., via octahedral tilting distortions) the conduction band narrows and the band gap increases. Decreasing the dimensionality from 3-D (e.g., the cubic perovskite structure) to 2-D (e.g., the K_2NiF_4 structure) does not significantly alter the band gap, whereas completely isolating the MO_6 octahedra (e.g., the ordered double perovskite structure) narrows the conduction band width dramatically and leads to a significant increase in the band gap. Inductive effects due to the presence of electropositive "spectator" cations (alkali, alkaline earth, and rare-earth cations) tend to be small and can generally be neglected.

Keywords: Oxides; Perovskites; Band structure calculations; Band gap; Electronic structure; Photocatalysis; d^0 transition metal ions; Structure-property relationships

1. Introduction

The electronic structure of a solid dictates its optical properties, electrical transport properties, and plays a major role in determining its reactivity and stability. Consequently, a quantitative understanding of the relationship between chemical bonding, crystal structure and electronic structure is a prerequisite for the rational design of optical, electronic and catalytic materials. These relationships have been studied extensively in compound semiconductors, and the principles that have emerged from this research are commonly used in the design of optoelectronic devices, such as LEDs, semiconductor lasers, photovoltaic cells, etc. On the other hand, detailed structure/bonding/property relationships are not understood at the same level of detail in oxides. Nonetheless, many technological and commercial applications are based on the optical, electronic and catalytic properties of semiconducting oxides. Important examples include transparent conductors, heterogeneous catalysts, pigments, and photocatalysts. Among these, developing new photocatalytic materials is perhaps the most challenging endeavor, as it entails controlling the optical band gap, carrier transport, catalytic activity, surface properties and chemical stability.

Photocatalysts have a number of applications including generation of hydrogen from water, environmental remediation and water treatment, self-cleaning windows and odor control. The "holy grail" of photocatalytic research is to find a material that can efficiently use sunlight to decompose water into hydrogen and oxygen [1,2]. The scientific community has been seeking this grail since it was first demonstrated that TiO_2 could photocatalytically decompose water over 30 years ago

*Corresponding author. Fax: +1-614-292-1362.
E-mail address: woodward@chemistry.ohio-state.edu (P.M. Woodward).

0022-4596/03/$ - see front matter © 2003 Elsevier Inc. All rights reserved.
doi:10.1016/S0022-4596(03)00289-5

[3]. Another very important application of photocatalysts is to oxidize organic contaminants and/or reduce heavy metal ion contaminants in water supplies. Such materials could be used in a wide range of applications, from waste water treatment to treating oil spills.

A good photocatalytic material must meet the following criteria: (a) an absorption spectrum that has significant overlap with the solar spectrum, (b) good "capacitance" of the electron–hole pair, (c) good redox ability, and (d) stability in water. Efficient usage of sunlight can only be achieved when the band gap is small enough so as to overlap with a sizeable fraction of the visible spectrum, which ranges from roughly 1.7 to 3.1 eV (740–400 nm). The capacitance of the electron–hole pair refers to a material's ability to keep the pair from readily recombining before performing the desired reduction–oxidation reactions at the surface. In order to achieve this, carrier transport must be efficient (the e^- and h^+ mobilities cannot be too small), and there should be some adsorption of charged species at the surface in order to induce band bending. The redox ability of a photocatalyst is related to the absolute position of the valence and conduction band edges, as illustrated in Fig. 1. Finally, stability of the material in aqueous media is a necessity when dealing either with the photocatalytic cleavage of water or with environmental remediation of contaminated water supplies. Despite a significant effort to improve upon the original, titanium dioxide is probably still the most effective and widely used photocatalyst, but its shortcomings include its band gap (over 3.0 eV) and the relatively low energy level of its conduction band edge. The large band gap of TiO_2 causes most of the solar spectrum to go unutilized, while the conduction band position tends to limit the rate of reduction at the surface, leading to an undesirably high rate of electron–hole recombination.

Clearly if one aspires to find or create a photocatalyst that improves upon the performance of TiO_2, one aspect of that quest is to understand how to optimize the position and width of the conduction band (CB). If the CB edge is too high in energy, a large band gap will result, and exposure to visible light will not create the needed electron–hole pairs. On the other hand, if the CB edge is energetically too low in energy, the rate of reduction reactions at the surface will plummet, and electron–hole recombination will dominate. For a binary d^0 transition metal oxide (M_yO_z), the orbital character of the valence band (VB) is primarily derived from oxygen $2p$ orbitals, with a progression from metal–oxygen bonding states at the bottom of the VB to oxygen non-bonding states at the top of the VB. The CB has strong metal d-orbital character, originating from the antibonding metal–oxygen interactions. In the ionic limit the VB to CB excitation can be described as an oxygen-to-metal charge transfer excitation.

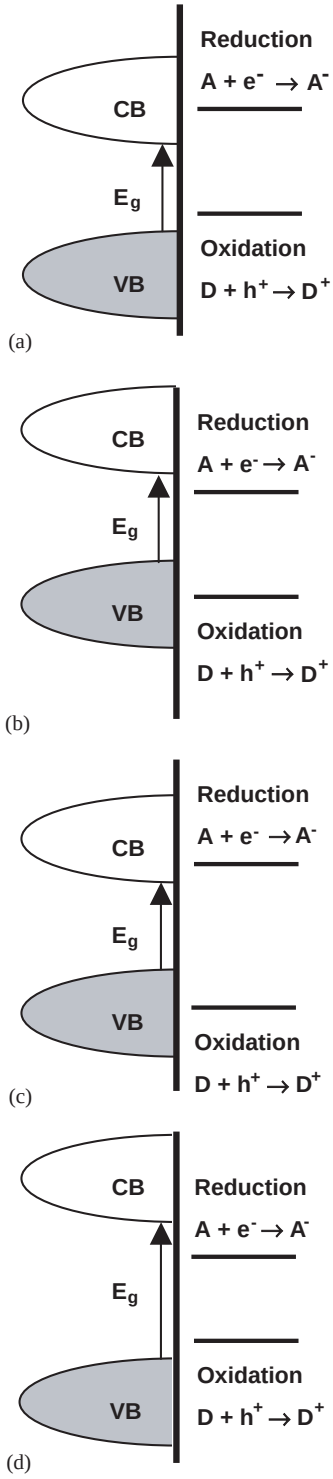

Fig. 1. Possible relationships between the semiconductor band positions and the surface redox reactions in photocatalysis. The figure depicts the following scenarios: (a) the conduction band (CB) is not sufficiently energetic to facilitate reduction, (b) the valence band (VB) is not correctly positioned to facilitate oxidation, (c) both CB and VB are improperly positioned, (d) both CB and VB are energetically positioned to favor oxidation and reduction reactions at the surface. In cases (a), (b) and (c) the excess concentration of electrons and/or holes causes carrier recombination to dominate and photocatalytic efficiency to sharply decline.

While the electronic properties of binary d^0 metal oxides have been studied fairly extensively, the electronic properties of ternary $A_xM_yO_z$ oxides, where A is an electropositive cation such as an alkali, alkaline-earth or rare-earth ion, are far from being completely characterized and understood. In these compounds the electropositive character of the A-site ions minimizes its contribution to electronic states near the Fermi level, E_F. However, the introduction of inert or "spectator" ions inevitably leads to a structural modification of the M_yO_z framework. For example, by changing the radius of the A-site cation one can modify the M–O–M bond angles (e.g., $SrTiO_3$ to $CaTiO_3$ to $Y_2Ti_2O_7$), the polyhedral connectivity (e.g., $SrTiO_3$ to Sr_2TiO_4), the cation coordination environment (e.g., $SrTiO_3$ to $BaTiO_3$) or a combination of the three (e.g., $SrTiO_3$ to $MgTiO_3$ to $Na_2Ti_3O_7$). This provides a mechanism for indirectly modifying the electronic structure through the use of spectator ions.

Since the VB to CB transition is largely an oxygen-to-metal charge transfer excitation, one might expect the size of the band gap would depend primarily on the electronegativity and coordination environment of the transition metal ion. However, you do not have to look beyond the binary oxides to realize this picture is an oversimplification. A glance at the optical absorption spectra of the binary d^0 oxides (Fig. 2a) clearly shows

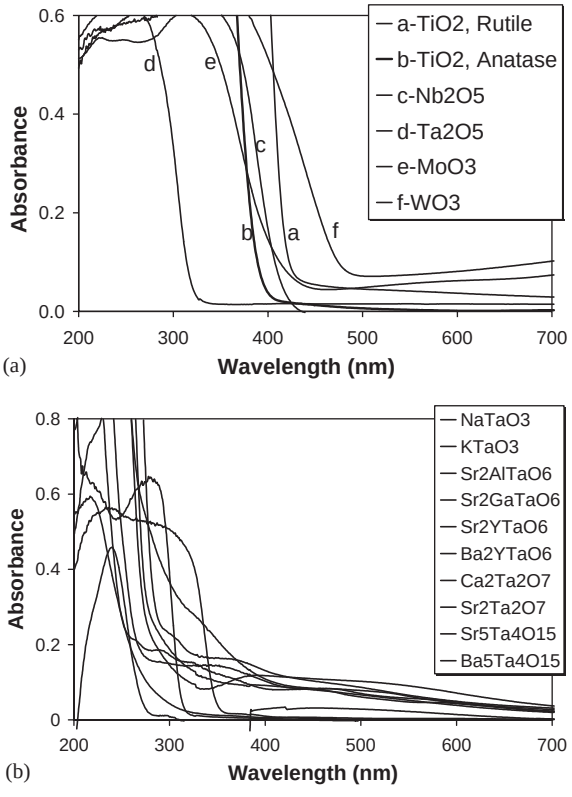

Fig. 2. (a) Diffuse reflectance spectra of binary d^0 transition metal oxides. (b) Diffuse reflectance spectra of oxides containing Ta^{5+} in octahedral coordination.

that cation electronegativity is only one factor that must be considered. Otherwise, how can you account for the different band gaps of the TiO_2 polymorphs? What electronegativity scale rationalizes the fact that WO_3 has a smaller gap than MoO_3, whereas Nb_2O_5 has a smaller gap than Ta_2O_5? The complexity of isolating one or two factors, among the many that impact the band gap, is also revealed in Fig. 2b, where the optical spectra of a series of oxides containing octahedrally coordinated Ta^{5+} are shown. Clearly there is a strong correlation between the electronic structure and the crystal structure.

The motivation of this study was to answer the following questions. What are the relative electronegativities of d^0 transition metal ions from groups 4, 5 and 6? The traditional electronegativity scales (Pauling, Allred–Rochow, Sanderson, etc.) are not in full agreement on this question. If we maintain a fairly reproducible local octahedral coordination environment about the transition metal ion, in what ways do secondary changes in structure (changes in M–O–M angles or connectivity of the octahedra) impact the electronic band structure? Do the spectator cations play a role beyond modification of the M_yO_z network? That is to say, can we find evidence for spectator cation inductive effects? Answers to these questions provide a framework for intelligent design of oxides for optical, electronic and/or catalytic applications. Our approach is to examine the optical properties of a relatively large family of compounds where the local transition metal ion environment is consistently the same. This involves studying a number of compounds that in isolation are perhaps not of great interest, but when the results are examined comparatively these measurements provide significant insight. We have supplemented the experimental measurements with band structure calculations in an attempt to identify the key features of bonding and structure that couple strongly with the electronic structure near the Fermi level. A side product of this effort is an evaluation of the accuracy and shortcomings of the band structure calculations themselves.

2. Experimental

2.1. Calculations

The band dispersion and density of states calculations were carried out using primarily version 47 of the Stuttgart tight binding, linear muffin tin orbital, atomic sphere approximation (TB-LMTO-ASA) code. The TB-LMTO-ASA method, or LMTO for short, is a self-consistent, density functional theory code, which incorporates scalar-relativistic corrections. In order to help identify the orbital interactions that are responsible for the electronic band structure, extended Hückel

tight-binding (EHTB) calculations were also utilized to a lesser extent. These calculations were performed using version 1.0 of the program Crystal And Electronic Structure AnalyzeR (CAESAR).

Detailed descriptions of the ab initio calculations using the LMTO method are given elsewhere [4,5]. The unit-cell volume is automatically separated into atomic and empty spheres, with the overlap between the spheres not exceeding 16%. The empty spheres consist of 1*s* orbitals and downfolded 2*p* orbitals, i.e., the 2*p* orbitals carry charge but do not contribute to the Hamiltonian and overlap matrices. Close-packed structures, such as cubic perovskites, did not necessitate the use of empty spheres. The default number of irreducible *k*-points was used in all calculations. The calculations were implemented using two combinations of local exchange correlation and oxygen valence orbitals: (1) the von Barth–Hedin exchange [6] with oxygen 2*p* and downfolded 3*s* orbitals, and (2) the Perdew–Wang exchange [7] with oxygen 2*s* and 2*p* orbitals. Unless specifically stated otherwise, the Perdew–Wang exchange function was utilized throughout the manuscript, due to the fact that it leads to noticeably better agreement with experimentally measured band gaps. So-called 'fat-band' representations were used to ascertain orbital contributions to bands near the Fermi energy.

The CAESAR package for Windows was developed by Ren et al. [8]. The program uses semi-empirical extended Hückel methods, which neglect electron–electron repulsion. EHTB tends to be less accurate than the LMTO calculations, but it can be useful for ascertaining the atomic orbital contributions to the particular bands, in a qualitative sense [9,10].

2.2. Synthesis

Table 1 lists the synthetic method, space group, final annealing temperatures and any impurities identified from the X-ray powder diffraction data for all samples synthesized during this study. $ATaO_3$ and $ANbO_3$ ($A = K, Na$) were used as obtained from Cerac and Alfa Aesar, respectively. Most of the remaining samples were prepared in polycrystalline form using conventional ceramic methods. Stoichiometric amounts of the appropriate metal oxides and alkaline earth carbonates were weighed and ground in an agate mortar and pestle using acetone to aid in mixing. The reaction mixtures were then preheated in a high form alumina crucible at 900°C for 8–12 h to decompose carbonate reagents. The preheated powders were then reground and heated until single-phase products were obtained. The samples were heated to the final annealing temperatures for a minimum of 12 h, with some samples requiring extended cycles of grinding and heating. In some samples small levels of impurities (a few percent on a mole basis) persisted, as noted in Table 1. In those cases the optical band gaps of the impurity phases were measured in order to ensure that the primary band gap transition in the diffuse reflectance spectrum was associated with the (majority) phase of interest.

$Sr_2M'MO_6$ ($M' = Al, Ga; M = Nb, Ta$) samples were obtained by the flux/anneal method described by Woodward et al. [11]. Stoichiometric amounts of $SrCO_3$ and the appropriate metal oxides were mixed intimately and preheated as described earlier. Next the reaction mixture was mixed thoroughly with the $SrCl_2$ fluxing reagent (in a 1:1 mole ratio of $SrCl_2$ to $SrCO_3$), then heated to 900°C for 12 h. The fluxing material was removed using dilute HNO_3, and the product was filtered, dried, and heated to its final annealing temperature.

Polycrystalline samples containing Y and Sc on the M'-site were prepared by heating a stoichiometric amount of a precursor $M'MO_4$ ($M' = Y, Sc; M = Nb, Ta$) intimately mixed with the desired alkaline earth carbonate. The precursors were made by heating their constituent oxides between 1200 and 1400°C, respectively [12,13]. Impurity levels in the A_2YMO_6 compounds were further reduced by additional heating of the double perovskite powders in an appropriate alkaline earth chloride molten salt flux.

The phase purity of each sample was confirmed by X-ray powder diffraction using a Bruker D8 Advance diffractometer equipped with an incident beam Ge monochromator and a Braun position sensitive detector. Data were collected from 15° to 120° 2θ ($\sim 0.014°$ step size, 1–2 s/step) using monochromatic Cu$K\alpha_1$ radiation (40 kV, 50 mA). For those compounds where an accurate crystal structure had not previously been reported, Rietveld refinements were performed to determine the crystal structure. Crystallographic details will be reported in a separate paper.

2.3. Diffuse reflectance measurements

The band gaps of the materials investigated in this study were measured from polycrystalline samples using diffuse reflectance spectroscopy, a method unaffected by temperature and surface defects [14]. Reflectance data were collected and converted to absorbance using a Perkin-Elmer Lambda 20 scanning double-beam spectrometer equipped with a 50 mm Labsphere integrating sphere over the spectral range 200–1100 nm (6.2–1.1 eV). The band gap energies quoted in this study are based on Shapiro's method [15] of extrapolating the onset of absorption to the wavelength axis. An alternative method of determining band gaps by Davis and Mott [16] was not used because identification of the transitions was difficult to resolve. This method involves solving Eq. (1) for the band gap energies in the appropriate linear region, where $E_{g,opt}$ is the direct (or indirect) band gap energy; α is the absorption

Table 1
Space groups, synthesis route, final annealing temperatures and impurities

Compound[a]	Synthesis Route (Temp, °C)[b]	Impurities[c]	Compound[a]	Synthesis Route (Temp, °C)[b]	Impurities[c]
$CaTiO_3$ [27]	Conv (1400)	None	Sr_2GaTaO_6 [33]	F/A (1500)	None
$Ca_3Ti_2O_7$ [23]	Conv (1400)	None	Sr_2YTaO_6 [20,28]	$M'M$ (1400)	Y_2O_3
$Ca_4Ti_3O_{10}$ [23]	Conv (1400)	None	Ba_2YTaO_6 [29]	$M'M$ (1400)	Y_2O_3
$SrTiO_3$ [25]	Conv (1400)	None	Sr_2MgMoO_6	Conv (1350)	$SrMoO_4$
Sr_2TiO_4 [24]	Conv (1400)	None	Ba_2MgMoO_6	Conv (1350)	$BaMoO_4$
$Sr_3Ti_2O_7$ [23]	Conv (1500)	None	Sr_2CaMoO_6	Conv (1300)	$SrMoO_4$
$Y_2Ti_2O_7$ [30]	Conv (1500)	None	Ba_2CaMoO_6	Conv (1300)	$BaMoO_4$
La_2MgTiO_6	Conv (1600)	Unknown[d]	Sr_2ZnMoO_6	Conv (1300)	$SrMoO_4$
Sr_2AlNbO_6 [20,31–33]	F/A (1400)	$Sr_5Nb_4O_{15}$	Ba_2ZnMoO_6	Conv (1200)	$BaMoO_4$
Sr_2GaNbO_6 [33]	F/A (1400)	$Sr_2Nb_2O_7$	Sr_2MgWO_6	Conv (1350)	$SrWO_4$
Sr_2YNbO_6 [34]	$M'M$ (1400)	Y_2O_3	Ba_2MgWO_6	Conv (1350)	$BaWO_4$
Ba_2YNbO_6 [35]	$M'M$ (1400)	Y_2O_3, Nb_2O_5	Ca_3WO_6	Conv (1200)	$CaWO_4$
Ca_2ScNbO_6 [36]	$M'M$ (1400)	None	Sr_2CaWO_6	Conv (1300)	$SrWO_4$
Sr_2ScNbO_6 [36]	$M'M$ (1400)	None	Ba_2CaWO_6	Conv (1300)	$BaWO_4$
Ba_2ScNbO_6 [36]	$M'M$ (1250)	None	Sr_2ZnWO_6	Conv (1200)	$SrWO_4$, ZnO
Sr_2AlTaO_6 [20,32,33]	Conv (1500)	None	Ba_2ZnWO_6	Conv (1200)	$BaWO_4$, ZnO

[a] The references listed in the table refer to reported crystal structure for each compound.
[b] Conv refers to conventional solid state synthesis method, F/A refers to synthesis in a molten alkaline earth chloride flux, and $M'M$ refers to conventional solid state synthesis from $MM'O_4$ and ACO_3.
[c] The band gaps (in eV) of the impurities are Y_2O_3 (4.9), Nb_2O_5 (3.0), ZnO (3.0), $SrMoO_4$ (3.8), $BaMoO_4$ (4.0), $SrWO_4$ (3.9), $BaWO_4$ (3.8), $CaWO_4$ (4.1), $Sr_5Nb_4O_{15}$ (3.9), and $Sr_2Nb_2O_7$ (3.7).
[d] Trace (<5%) impurities could not be identified from the X-ray powder diffraction data, as the reflections related to the impurity phases were too weak to identify the compound.

coefficient; B is a constant; and n is 1/2 for direct gap material or 2 for indirect gap material. With the compounds investigated in this study this method of analysis tended to give a linear fit over a limited range of photon energies, using either a direct $(n = 1/2)$ or an indirect $(n = 2)$ gap. This leads to ambiguity in proper interpretation of the data. Part of the difficulty may lie in the fact that according to our LMTO calculations, the bands at the top of the VB are rather flat so that direct and indirect transitions should occur at very similar energies:

$$\alpha h\upsilon = B(h\upsilon - E_{g,opt})^n. \quad (1)$$

3. Methodology

As discussed earlier, the band gap is sensitive to a variety of factors that relate back to the composition and structure. Isolating the influence of individual changes in the structure and/or composition can be difficult, due to unavoidable correlation between parameters. While making one structural change, for example going from $SrTiO_3$ to $CaTiO_3$ in order to change the Ti–O–Ti bond angle, we may introduce inductive effects originating from the greater electronegativity of the Ca^{2+} ion, or trigger a distortion of the TiO_6 octahedron. The influence of these secondary effects will be convoluted with the primary effect, in this case changing the Ti–O–Ti angle. This secondary effect can make it difficult to discern the relationship between the primary variable and the electronic structure in a quantitative fashion. Because theoretical calculations can be performed on idealized structures, or even on hypothetical compounds, they provide an opportunity to deconvolute the effect of the primary variable from other influences. Furthermore, calculations give direct information regarding the positions and the widths of the conduction and valence bands, as well as the bonding interactions responsible for these bands. These parameters are difficult to measure experimentally. For these reasons band structure calculations were a useful supplement to the diffuse reflectance measurements.

Almost all of the compounds examined in this study adopt either perovskite or perovskite-related structures. Perovskites were chosen as the basis of this study for several reasons. First of all, ions from across the periodic table can be incorporated into the perovskite structure. Secondly, the octahedral coordination of the transition metal ion is usually rather symmetric and reproducible from one compound to the next. Finally, numerous substitutions and structural modifications can be used to alter the electronic structure. We begin the discussion by considering ordered double perovskite compounds where the d^0 transition metal ion centered octahedra are isolated from each other as a way of evaluating the oxygen-to-metal charge transfer energy and how it varies from one transition metal ion to the next. Next the calculated band structures of cubic AMO_3 ternary perovskites are presented, in order to

show how the picture changes when the width of the conduction band must also be taken into consideration. Finally, we explore how distortions of the M–O–M bond angles and changes in the polyhedral connectivity impact the electronic structure.

Ordered double perovskites have the formula $A_2M'MO_6$ where the M and M' cations are octahedrally coordinated by oxygen anions (see Fig. 3). In the aristotype cubic structure, the highly electropositive A cation is coordinated to twelve oxygens, while the MO_6 and $M'O_6$ octahedra share corners in an ordered pattern analogous to the rock salt structure. In the cubic structure the M–O–M' bond is linear, whereas, in lower symmetry structures the M–O–M' angle distorts away from 180° and the A-site coordination polyhedron becomes distorted. For the compounds studied in this paper, M is the d^0 transition metal of interest (Ti^{4+}, Nb^{5+}, Ta^{5+}, Mo^{6+} or W^{6+}), while M' and A are lower valent electropositive ions. Fig. 4 shows the calculated electronic density of states and full band structure near the Fermi level for the ternary perovskite $KTaO_3$ and its double perovskite analog Sr_2AlTaO_6. The features of the $KTaO_3$ band structure (as well as $SrTiO_3$ shown later in Fig. 13) are in good agreement with previous calculations on d^0 transition metal perovskite oxides [17,18]. The fat band representations, shown in Fig. 4, reveal that the conduction band originates from the antibonding π interaction between the Ta t_{2g} and O $2p$ orbitals in both compounds, as expected. Orbital overlap diagrams between the Ta d_{xy} and O $2p$ orbitals at the Γ and M points can be constructed from the coefficients of the extended Hückel calculations. These diagrams are shown in Fig. 5. The conduction band minimum falls at the Γ point, because at that point in k-space translational symmetry dictates that the net interaction between oxygen $2p$ π orbitals and the Ta t_{2g} orbitals is nonbonding. In contrast, at the M point oxygen interacts with both of its tantalum neighbors in an antibonding fashion. The contrast between the nonbonding and antibonding interactions dictates the width of the t_{2g} conduction band.

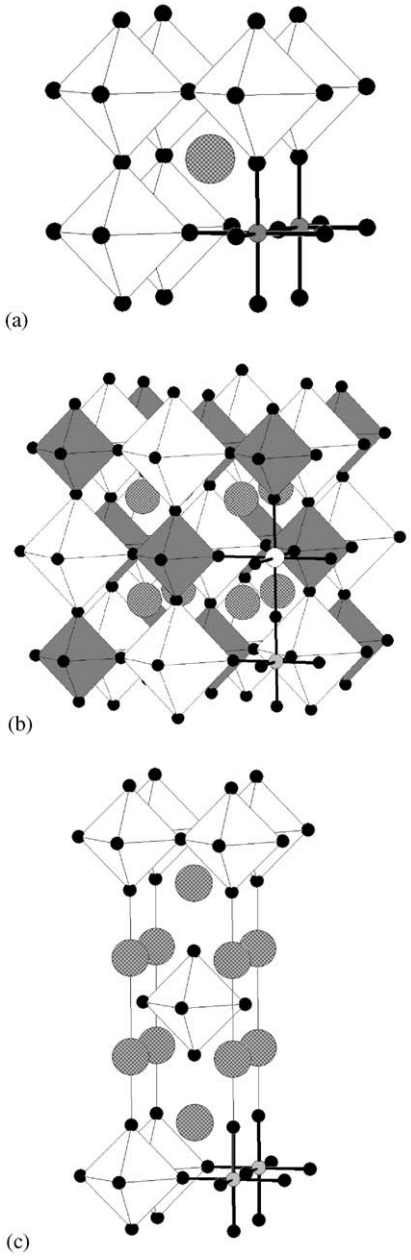

Fig. 3. Structural depiction of (a) the simple perovskite $SrTiO_3$, (b) the ordered double perovskite Sr_2AlTaO_6, and (c) the Ruddleson–Popper phase Sr_2TiO_4.

The orbital overlap diagram for Sr_2AlTaO_6 at the Γ and M points is also shown in Fig. 5. In the double perovskite structure each oxygen atom is coordinated to a single tantalum ion, so that translational symmetry does not prevent antibonding overlap at both Γ and M points. While it is true that across a face diagonal of the unit cell the Ta–Ta and O–O orbitals have slight bonding and antibonding character at the Γ and M points, respectively, the spatial overlap is poor and these interactions are expected to be very weak. The net result is a very narrow conduction band. Consequently, the band gap of an ordered double perovskite should be an accurate indicator of the oxygen-to-metal charge transfer energy.

4. Results and discussion

4.1. Ordered double perovskites

Ordered double perovskite are considered first in order to compare the charge transfer energies of the five transition metals. For the purpose of calculations, the structures of the double perovskites were generated using the program SPuDS [19]. SPuDS has been shown to be quite accurate at predicting structures of perovskites, and the use of calculated structures has

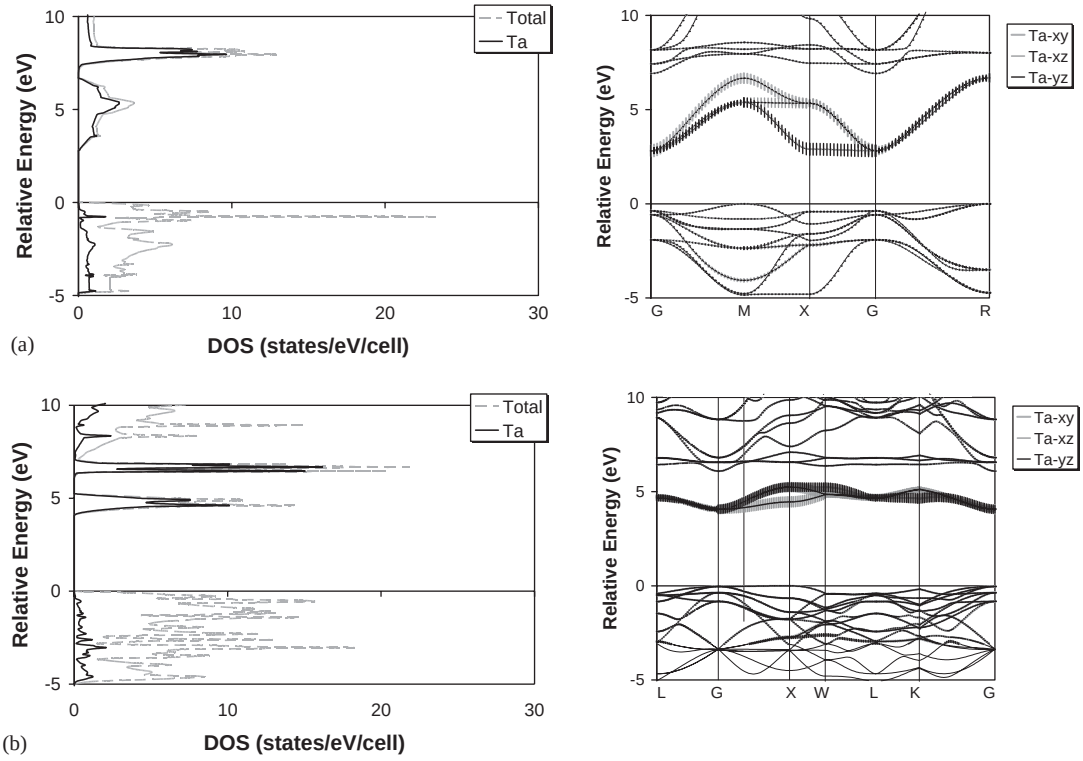

Fig. 4. Density of states (DOS) and band structures diagrams for (a) $KTaO_3$ and (b) Sr_2AlTaO_6. The total electronic DOS is shown in black and the partial DOS of Ta in red. The hatching in the band structure diagram shows the orbital contributions to each band (Ta t_{2g} fat bands). The t_{2g} width of the double perovskites is quite narrow, and as such, is a good indicator of the oxygen to metal charge transfer energy.

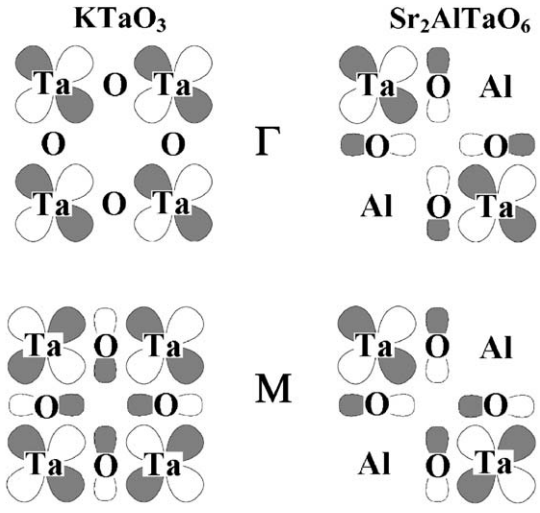

Fig. 5. Ta d_{xy}–O $2p$ π overlap at the Γ and M points in both $KTaO_3$ and Sr_2AlTaO_6. The changes in overlap makes the t_{2g} band wide in a simple perovskite and narrow in the double perovskite.

the advantage that a given metal–oxygen distance (e.g., Ta–O) remains absolutely constant from one compound to the next. The results of the LMTO calculations on ordered double perovskites are shown in Fig. 6 and in Tables 2 and 3.

Fig. 6a shows the variation in the position and width of the conduction band for a number of double perovskites containing Ta^{5+}. As expected the conduction band widths are quite narrow ($\sim$0.9–1.6 eV). The similar band gaps obtained for Sr_2AlTaO_6 and Ba_2YTaO_6 imply that direct Ta–Ta overlap across the face of the simple perovskite unit cell is negligible. Such interactions are known to influence magnetic ordering in some perovskites, but here the electronic structure shows little response to a significant change in the Ta–Ta distance, 5.46 Å in Sr_2AlTaO_6 and 6.03 Å in Ba_2YTaO_6. The implication is that this interaction does not contribute significantly to the optical and/or electrical transport properties. The similar results obtained for La_2LiTaO_6 and Sr_2YTaO_6 imply that changing the oxidation state of the A and M' cations does not have a significant impact on the band gap. Finally, we note that the band gaps and CB widths of $A_2M'TaO_6$ compounds can be separated into two groups: cubic double perovskites (4.0–4.1 eV) and distorted double perovskites (4.4–4.6 eV). Within each group, the band gap is relatively insensitive to substitutions on either the A or M' cation sites. However, the occurrence of an octahedral tilting distortion (typically lowering the symmetry from cubic to monoclinic) increases the band gap by $\sim$0.5 eV. Since the

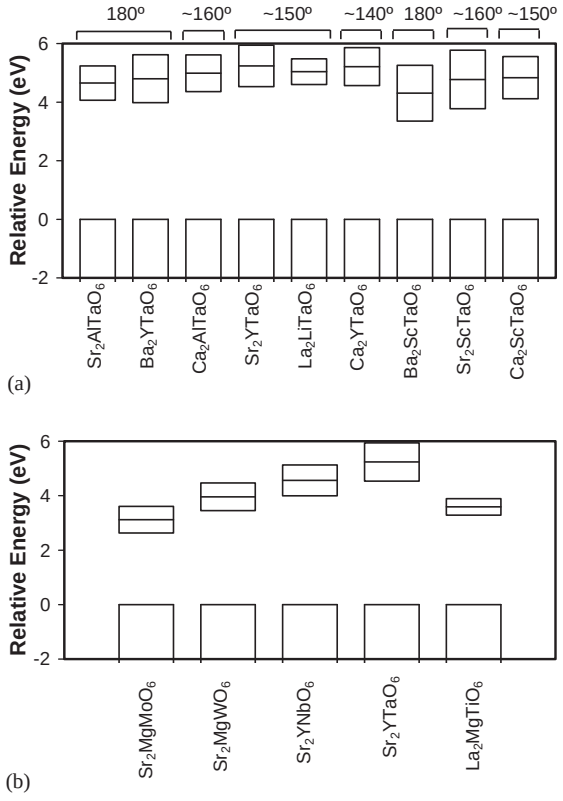

Fig. 6. Conduction band and valence band positions and widths from LMTO calculations of the ordered double perovskites of (a) Ta and the (b) five transition metals. Midpoints of the t_{2g} bands are marked. Only the valence band and t_{2g} conduction bands are shown for clarity. The approximate Ta–O–Ta bond angles are labeled at the top of (a).

conduction band width is rather small, even in the cubic double perovskites such an effect was neither anticipated nor is it easy to explain.

The A_2ScTaO_6 compounds are grouped together in Table 2 and Fig. 6, because the calculations suggest that the electronic structure of these compounds differ somewhat from the others. The band gaps are smaller, and the conduction band width is larger. Furthermore, both parameters are sensitive to changes in octahedral tilting. The partial density of states diagrams (PDOS) displayed in Fig. 7 show that the M' cations make almost no contribution to the t_{2g} conduction band when M' is a main group ion such as Al^{3+} or Li^{+}. This effect stems from the fact that the symmetry of the valence s-orbitals are not appropriate for mixing with the Ta–O π^* orbitals of the ordered double perovskite structure. In the PDOS diagram for Sr_2YTaO_6 we see some hybridization between the Y 4*d* orbitals and the Ta–O t_{2g} orbitals. The mixing is small because the energetic overlap is still poor. Consequently, the Y contribution to the conduction band is small. On the other hand, the PDOS plot shown in Fig. 7d reveals that both Ta^{5+} and Sc^{3+} make nearly equivalent contributions to the conduction band. Thus, the electronically active TaO_6 octahedra are not truly isolated (in an electronic sense) in the A_2ScTaO_6 compounds, and the electronic structure of these compounds is intermediate between a zero-dimensional ordered double perovskite and a three-dimensional ternary perovskite. Perhaps this viewpoint is not surprising as the Ta^{5+} and Sc^{3+} ions are

Table 2
Results of band structure calculations on $A_2M'TaO_6$ ordered double perovskites[a]

Compound	Space group	M–O–M' (°)	E_g (eV)	$W_{t_{2g}}$ (eV)	Mid-t_{2g} (eV)[b]
Sr_2AlTaO_6	*Fm*3*m*	180	4.07	1.17	4.65
Ba_2YTaO_6	*Fm*3*m*	180	3.99	1.64	4.80
Ca_2AlTaO_6	$P2_1/n$	160	4.36	1.25	4.99
Sr_2YTaO_6	$P2_1/n$	151	4.53	1.41	5.24
La_2LiTaO_6	$P2_1/n$	151	4.60	0.88	5.04
Ca_2YTaO_6	$P2_1/n$	141	4.56	1.30	5.21
Ba_2ScTaO_6	*Fm*3*m*	180	3.35	1.90	4.31
Sr_2ScTaO_6	$P2_1/n$	160	3.78	2.00	4.78
Ca_2ScTaO_6	$P2_1/n$	148	4.11	1.45	4.84

[a] Structures created using SPuDS [19], where the Ta–O distance was held constant at 1.987 Å in all compounds.
[b] Mid-t_{2g} is the energy difference between the midpoint of the t_{2g} band and the top of the valence band.

Table 3
Measured and calculated band gaps for various ordered double perovskites[a]

Compound	M–O (Å)	M–O–M' (°)	Meas. E_g (eV)	Calc. E_g (eV)	$W_{t_{2g}}$ (eV)	Mid-t_{2g} (eV)[b]
La_2MgTiO_6	1.965 × 6	154	3.9	3.29	0.60	3.59
Sr_2YTaO_6	1.987 × 6	151	4.7	4.53	1.41	5.24
Sr_2YNbO_6	1.978 × 6	151	3.9	4.00	1.13	4.56
Sr_2MgWO_6	1.917 × 6	165	3.6	3.45	1.01	3.96
Sr_2MgMoO_6	1.907 × 6	166	2.7	2.63	0.98	3.12

[a] Structures created using SPuDS [19].
[b] Mid-t_{2g} is the energy difference between the midpoint of the t_{2g} band and the top of the valence band.

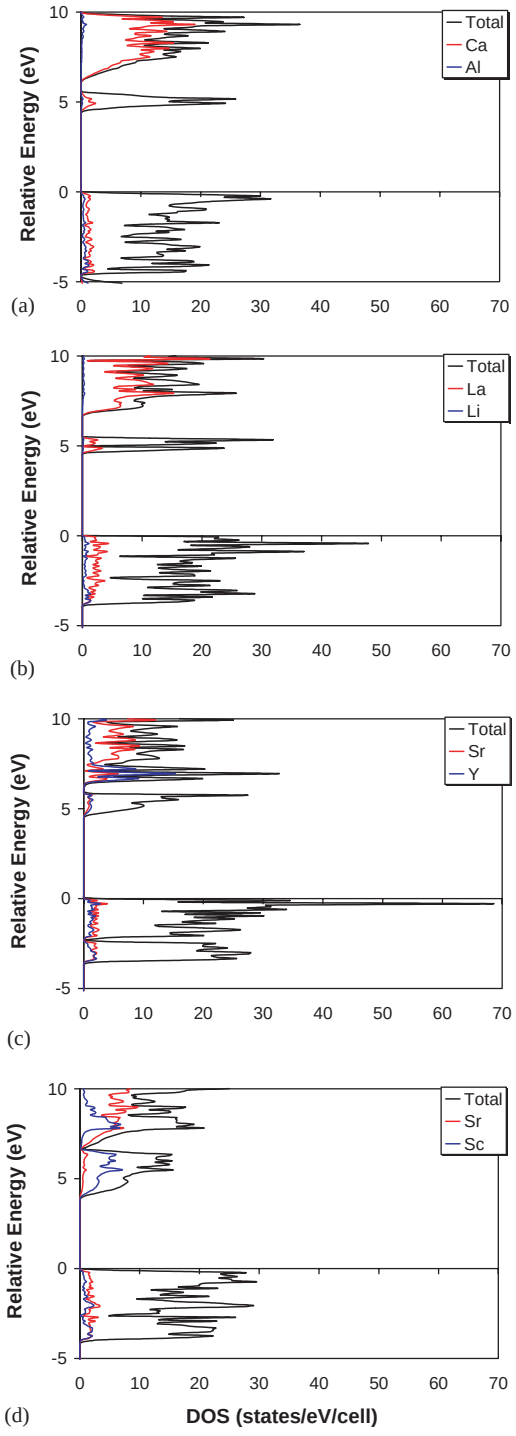

Fig. 7. Total and partial density of state as obtained from LMTO calculations for the A and M' cations in (a) Ca_2AlTaO_6, (b) La_2LiTaO_6, (c) Sr_2YTaO_6, and (d) Sr_2ScTaO_6.

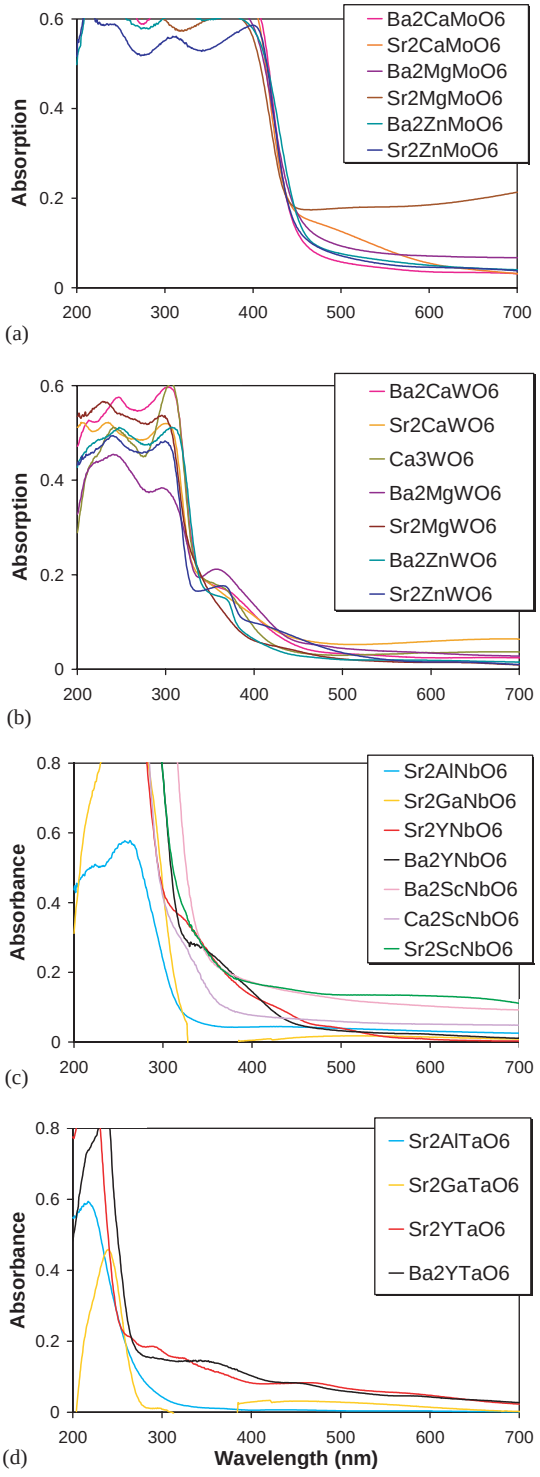

Fig. 8. Diffuse reflectance spectra for (a) Mo, (b) W, (c) Nb, and (d) Ta ordered double perovskites. Pre-absorption edge features are discussed briefly in the text. Sr_2GaMO_6 (M = Nb, Ta) exhibits a very weak photoluminescence.

located diagonal from each other on the periodic table, and therefore, might be expected to have similar electronegativities. This picture of their electronic structure also explains the sensitivity of the A_2ScTaO_6 band gap to octahedral tilting, through the conduction band width.

The diffuse reflectance spectra for a large number of ordered double perovskites are shown in Fig. 8. Numerical values for the band gaps are given in Table 4. These results confirm that the effects of the A and M' cations are minimal in most cases. The band

Table 4
Measured band gaps for ternary and ordered double perovskites

Compound	E_g (eV)	Compound	E_g (eV)	Compound	E_g (eV)
Ternary perovskites					
$SrTiO_3$[a]	3.1	$KNbO_3$	3.1	$KTaO_3$[a]	3.5
$CaTiO_3$[a]	3.3	$NaNbO_3$	3.4	$NaTaO_3$[a]	4.0
Ordered double perovskites					
La_2MgTiO_6	3.9	Sr_2AlTaO_6	4.6	Sr_2ZnMoO_6	2.7
Sr_2AlNbO_6	3.8	Sr_2GaTaO_6	4.5	Ba_2ZnMoO_6	2.7
Sr_2GaNbO_6	3.8	Sr_2YTaO_6	4.7	Sr_2MgWO_6	3.6
Sr_2YNbO_6	3.9	Ba_2YTaO_6	4.6	Ba_2MgWO_6	3.4
Ba_2YNbO_6	3.8	Sr_2MgMoO_6	2.7	Ca_3WO_6	3.6
Ca_2ScNbO_6	4.1	Ba_2MgMoO_6	2.7	Sr_2CaWO_6	3.6
Sr_2ScNbO_6	3.9	Sr_2CaMoO_6	2.7	Ba_2CaWO_6	3.6
Ba_2ScNbO_6	3.6	Ba_2CaMoO_6	2.7	Sr_2ZnWO_6	3.7
				Ba_2ZnWO_6	3.5

[a] Band gaps from literature (in eV): $SrTiO_3$ (3.22, 3.3) [37,18], $CaTiO_3$ (3.5) [38], $KTaO_3$ (3.6) [39], $NaTaO_3$ (4.0) [39].

gaps for all six molybdenum compounds investigated were found to be nearly identical ($E_g \sim 2.7$ eV); while only slightly more variation is seen among seven tungsten containing ordered double perovskites ($E_g \sim 3.6$ eV). The variation from one compound to the next increases somewhat as the electronegativity of the d^0 ion decreases, but the seven niobium compounds ($E_g \sim 3.8$ eV) and four tantalum compounds ($E_g \sim 4.6$ eV) each fall within a fairly tight group. In some cases pre-edge absorption features can be seen. These features are particularly prevalent in the ordered double perovskites containing W^{6+}. Our spectroscopic tools are not sophisticated enough to unambiguously identify the origins of these features. In some cases it is possible that they can be attributed to small levels of secondary phases (e.g., ZnO in A_2ZnWO_6 and Nb_2O_5 in Ba_2YNbO_6), while in other cases careful X-ray powder diffraction analysis indicates that there are no secondary phases present. Excitations to or from defect states in the band gap are a possibility. Another possible explanation is the presence of bound excitons. Comparison of these results with the calculations discussed above is interesting. It is important to note that for most of the cases shown in this figure there is almost no difference between the band gaps of cubic and distorted $A_2M'MO_6$ perovskites. Thus, we conclude that the "cubic" effect is an artifact of the calculations. Recall that LMTO calculations require empty spheres in the distorted perovskites that are not required for, and cannot be incorporated into, the cubic structures. On the other hand, one can clearly see that among the A_2ScNbO_6, and to a lesser extent with the A_2YNbO_6 compounds, the band gap increases with increased octahedral tilting. This is consistent with the idea that emerged from the calculations, namely that the valence d-orbitals of Y^{3+} and particularly Sc^{3+} can mix electronically into the conduction band. The effect is expected to be somewhat smaller with $M = Nb^{5+}$ than with $M = Ta^{5+}$, because of the increased electronegativity of the Nb^{5+} ion.

Having confirmed that the band gap for the ordered double perovskites is relatively insensitive to changes in the A and M' cations, or the structure, we can now look at the influence of changing the identity of the d^0 ion. Fig. 6b and Table 3 show the calculated band gaps and conduction band widths for isostructural double perovskites containing each of the five transition metals of interest. Each of the compounds listed in this table was purposefully chosen to be distorted from cubic symmetry, in order to avoid the "cubic" effect that appears to be an artifact of the calculations. With the exception of La_2MgTiO_6, where the calculated band gap is too small by 0.6 eV, the calculations and experimental results are in remarkably good agreement. Such agreement could only be obtained using the Perdew–Wang exchange correlation with oxygen 2s and 2p orbitals included in the calculation. Using the default von Barth–Hedin correlation yielded band gaps that were smaller by 1–2 eV. Both calculations and diffuse reflectance spectra show the band gap decreasing in the following manner: $Ta^{5+} > Nb^{5+} \sim Ti^{4+} > W^{6+} > Mo^{6+}$. The trend is for the band gap to decrease as you either move left to right across a row (also accentuated by increasing the oxidation state) or move up a column of the periodic table. The trends agree with the typical expectations for electronegativity based on effective nuclear charge considerations. It should be born in mind that the use of the term electronegativity here refers to the ease of oxygen-to-metal charge transfer for a transition metal ion in its highest oxidation state surrounded by an octahedron of oxygen. Highly charged transition metals are more electronegative than their less charged brethren, leading to a more covalent interaction with the neighboring oxygen, and therefore, a smaller band

gap. These values cannot be used to compare electronegativity of say Mo^{4+} to Nb^{4+} to Ti^{4+}. Throughout the remainder of the paper we will generally use the term effective electronegativity to avoid confusion.

The pentavalent ions Ta^{5+} and Nb^{5+} (as well as Mo^{6+}/W^{6+}) are often thought of as almost interchangeable, because they have nearly identical ionic radii and often times very similar crystal chemistry. The same can be said of Mo^{6+} and W^{6+}. However, these results show directly that the effective electronegativity of the 4*d* transition metal ions is higher than their 5*d* counterparts, and as a consequence they should be expected to form more covalent bonds with oxygen. This realization helps to rationalize differences in the physical properties, particularly dielectric properties, of isostructural tantalum and niobium analogues. For example, $KTaO_3$ is cubic with perfectly regular Ta^{5+} centered octahedra, whereas $KNbO_3$ is ferroelectric due to displacements of the Nb^{5+} ions from the center of their octahedra. It is well known that this cation shift originates from a second-order Jahn–Teller distortion, and the tendency for this distortion increases as the energy difference between the low lying metal t_{2g} orbitals and the oxygen 2*p* orbitals decreases. The effective electronegativity measured here is a direct experimental characterization of this energy separation, and the measurements unambiguously reveal a large difference between this value in Nb^{5+} and Ta^{5+} oxides. Finally, we note that along a diagonal of the periodic table, $W \rightarrow Nb \rightarrow Ti$, the band gaps are fairly similar. Thus, from an effective electronegativity standpoint diagonal similarity is more pronounced than among elements of the same group (IV, V or VI).

4.2. Ternary (cubic) perovskites

We now examine ternary AMO_3 perovskites to understand how band width effects modify the electronic structure. In a ternary perovskite the MO_6 octahedra are no longer isolated from each other, instead, they share corners in all three dimensions. The *M*–O–*M* angles are 180° in the cubic structure and distort from 180° in lower symmetry structures. The orbital overlap at the Γ point between the *M* *d* and O 2*p* orbitals is shown in Fig. 5, with the assumption again of a highly ionic *A* cation. The t_{2g} and e_g bands have the same π^* and σ^* character as in the double perovskites. However, these bands are now considerably wider as explained above and shown in Figs. 5 and 6. The results of the LMTO calculations for cubic AMO_3 perovskites are shown in Fig. 9 and in Table 5. As expected the t_{2g} band width is much wider, ranging from 2.8 eV in $SrTiO_3$ to 4.6 eV in WO_3. The size of the band gap follows essentially the same trend as observed in the ordered double perovskites, $Ta^{5+} > Nb^{5+} > Ti^{4+} > W^{6+} > Mo^{6+}$, showing that the effective cation electronegativity

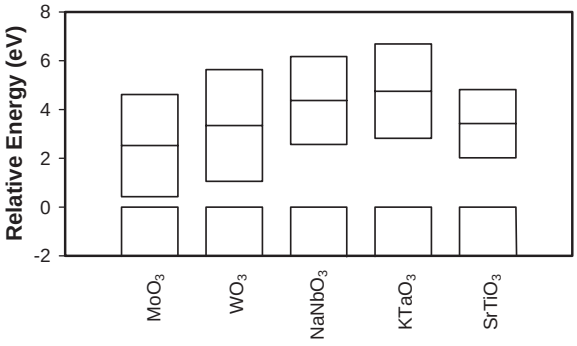

Fig. 9. Schematic diagram of conduction and valence band locations obtained from LMTO calculations for ideal ReO_3 structures in the case of MoO_3 and WO_3, and cubic in the case of $NaNbO_3$, $KTaO_3$ and $SrTiO_3$. Midpoints of the t_{2g} bands are marked. Only the valence band and t_{2g} conduction bands are shown for clarity.

remains an important factor in determining the band gap. However, the covalency of the *d* orbitals also changes the width of the conduction band and must be taken into consideration. The conduction band width increases as the oxidation state increases ($Nb^{5+} \rightarrow Mo^{6+}$; $Ta^{5+} \rightarrow W^{6+}$) due to increased energetic overlap between *M* t_{2g} and O 2*p* orbitals. It also increases as the principle quantum number of the valence *d* orbitals increases ($Nb^{5+} \rightarrow Ta^{5+}$; $Mo^{6+} \rightarrow W^{6+}$), presumably due to improved spatial overlap between *M* t_{2g} and O 2*p* orbitals. As a result, upon replacing a 4*d* ion with a more electropositive and less covalent 5*d* analogue, the increase in band gap for an AMO_3 perovskite is smaller than the increase observed for an analogous $A_2M'MO_6$ ordered double perovskite. This effect can only be understood once the effects of band width are taken into consideration.

Unlike the ordered double perovskites, with the ternary perovskites it is not possible to compare calculations and experimental results for all transition metal ions of interest. $SrTiO_3$ and $KTaO_3$ adopt the cubic perovskite structure at ambient conditions, but both $NaNbO_3$ and WO_3 undergo distortions involving octahedral tilting and displacements of the cation from the center of the octahedron. $KNbO_3$ does not show octahedral tilting, but does have a pronounced ferroelectric displacement of the Nb^{5+} ions. These distortions affect the band structure in a non-negligible manner. The thermodynamically stable form of MoO_3 does not exist with the corner sharing ReO_3-type connectivity. Keeping these limitations in mind, the values given in Table 5 show that the calculations consistently underestimate the band gap by $\sim$0.7–1.4 eV. Considering the fact that the experimental and calculated values agreed quite well among the ordered double perovskites, this result suggest that the LMTO calculations provide an accurate assessment of the charge transfer energy, but overestimate the band width. Fig. 10 shows the diffuse

Table 5
Measured and calculated band gaps of cubic ternary perovskites[a]

Compound	M–O (Å)	Meas. E_g (eV)	Calc. E_g (eV)	$W_{t_{2g}}$ (eV)	Mid-t_{2g} (eV)[b]
$SrTiO_3$[a]	1.953 × 6	3.1	2.02	2.80	3.42
$KTaO_3$	1.994 × 6	3.5	2.82	3.87	4.76
$KNbO_3$	1.979 × 6	3.1[c]	2.57	3.60	4.37
WO_3	1.917 × 6	2.4[d]	1.05	4.59	3.34
MoO_3	1.907 × 6	—	0.43	4.19	2.53

[a] Structures created using SPuDS [19], except for $SrTiO_3$ which was taken from Meyer et al. [25].
[b] Mid-t_{2g} is the energy difference between the midpoint of the t_{2g} band and the valence band.
[c] Actual structure is not cubic, but distorted by Nb^{5+} displacements. The band gap of a truly cubic compound would be smaller.
[d] Actual structure is not cubic, but distorted by octahedral tilting and W^{6+} displacements. The band gap of a truly cubic compound would be smaller.

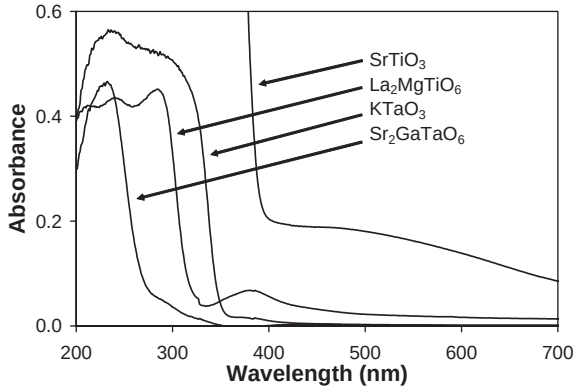

Fig. 10. The absorbances of simple perovskites (AMO_3) start at lower wavelengths (higher energy) than corresponding transition metal double perovskites ($A_2M'MO_6$).

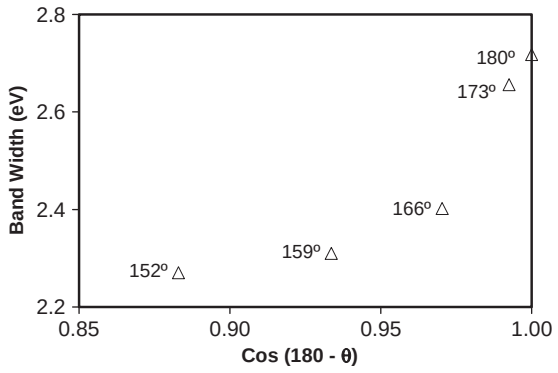

Fig. 11. The t_{2g} conduction band width for simulated $CaTiO_3$ perovskites as a function of Ti–O–Ti bond angle (°).

reflectance spectra of the Ti^{4+} and Ta^{5+} ions in cubic ternary perovskites in comparison with their ordered $A_2M'MO_6$ counterparts. The simple perovskites possess band gaps that are smaller by ~0.8 eV for titanium and ~1.2 eV smaller for tantalum, illustrating the significant impact that band width considerations can have on the band gap. The larger effect for Ta^{5+} is consistent with the larger width of the conduction band of $KTaO_3$ to begin with.

4.3. Distorted ternary perovskites

LMTO calculations were run on simulated $CaTiO_3$ perovskites with various Ti–O–Ti bond angles. The program POTATO [20] was used to create structures of $CaTiO_3$ with bond angles of 152°, 159°, 166°, 173° and 180°, while holding the Ti–O distances and O–Ti–O angles constant. All five structures were created using *Pnma* space group symmetry. Fig. 11 shows the relationship between the calculated width of the t_{2g} band, the calculated band gap, and the Ti–O–Ti bond angle. The band width decreases fairly sharply as a function of $\cos(180-\theta)$ as the bond angle deviates from 180° to 166°. In turn, the decreased conduction band width leads to a corresponding increase in the band gap. This $\cos(180-\theta)$ dependence of the band width has also been calculated and seen for e_g-derived bands [21]. LMTO calculations suggest that the band width decreases more gradually upon further distortion of the Ti–O–Ti angles. The origin of the effect stems from the fact that as the symmetry is lowered and the Ti–O–Ti bond angles distort the orbital overlap at the minimum energy point of the conduction band (at the Γ-point) is no longer perfectly non-bonding. As the distortion increases the antibonding character at the conduction band minimum increases. This destabilization of the conduction band decreases the width of the conduction band and increases the band gap. The magnitude of this effect, ~0.4–0.5 eV, is not inconsequential in comparison with the changes that occur upon changing transition metal ion, and cannot be neglected even in a semi-quantitative assessment of the electronic structure.

Fig. 12 shows the diffuse reflectance spectra for compounds with different M–O–M bond angles. The bond angles in the cubic perovskites of $SrTiO_3$ and $KTaO_3$ are 180°, whereas in the distorted perovskites $CaTiO_3$ and $NaTaO_3$ the angles are ~156°, and in the pyrochlore $Y_2Ti_2O_7$ the Ti–O–Ti angles are ~133°. As the bond angle decreases from 180° to 156° the band gap increases by ~0.2 and ~0.4 eV for the M = Ti and ~0.5 eV for M = Ta. The more pronounced effect seen

for tantalum stems once again from the fact that the conduction band is wider to begin with.

4.4. Layered compounds

Moving from a ternary perovskite to an ordered double perovskite effectively changes the dimensionality of the electronic structure from three to zero. The results discussed above show that this modification increases the band gap through reduction of the conduction band width. A less dramatic perturbation on the electronic structure can be achieved by changing the composition in such a way as to stabilize a layered perovskite phase, such as a Ruddlesden–Popper, Dion–Jacobson or Aurivillius phase. In order to investigate how this modification impacts the electronic structure we studied a series of $A_{n+1}Ti_nO_{3n+1}$ ($A = Sr, Ca$) Ruddlesden–Popper phases (see Fig. 3c) [22]. This reduces the dimensionality of the compound from three-dimensional ($n = \infty$) to pseudo-two-dimensional ($n > 1$) to effectively two-dimensional ($n = 1$) [23,24].

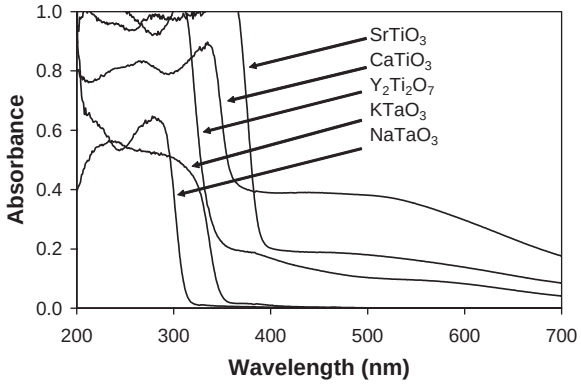

Fig. 12. Diffuse reflectance spectra illustrating the effect of distorting the M–O–M bonds.

Sr_2TiO_4 and $SrTiO_3$ represent two extremes of the Ruddlesden–Popper series. In order to probe the connectivity changes in isolation from other effects, an idealized structure of Sr_2TiO_4 was constructed where all Ti–O bond lengths were set equal to the Ti–O bond distances observed in $SrTiO_3$ (1.9525 Å) [25]. The calculated band structures are shown in Fig. 13. The Ti d_{xz} and d_{yz} bands are less disperse in Sr_2TiO_4 than in $SrTiO_3$ because the layering breaks the connectivity in the z-direction. Despite the narrowing of the d_{xz} and d_{yz} bands, the conduction band in Sr_2TiO_4 is nearly the same width as in $SrTiO_3$ because the interaction between the Ti d_{xy} and oxygen $2p$ orbitals remains essentially unaffected by the change in structure. The calculated band gaps of $SrTiO_3$ and the idealized Sr_2TiO_4 structure were 2.02 and 1.80 eV, respectively. This small change shows that changing dimensionality from three to two

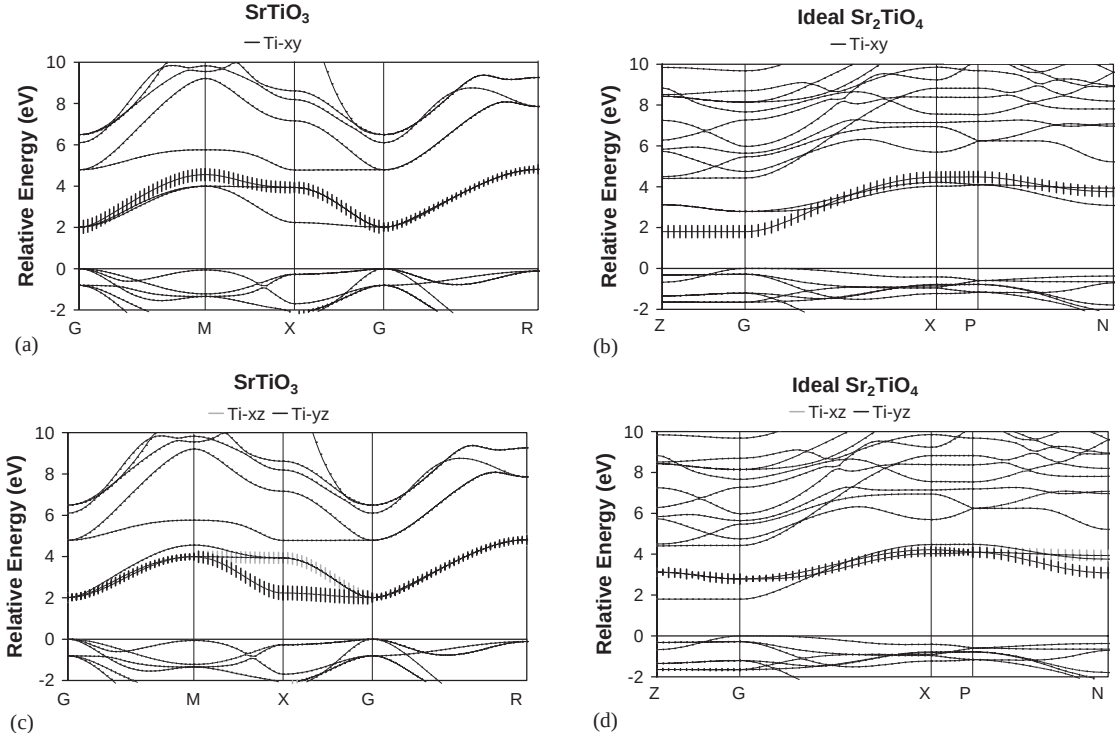

Fig. 13. Band structures of $SrTiO_3$ and idealized Sr_2TiO_4 (where the Ti–O distances are equal to the distances in $SrTiO_3$) showing the fat band representations of the t_{2g} orbitals. Energies are relative to the respective Fermi energies of the compounds. (a) and (b) show the Ti d_{xy} band has approximately the same width for both compounds (2.80 and 2.68 eV, respectively), leading to similar band gaps, whereas, the Ti d_{xz} and d_{yz} bands in both compounds do narrow with reduction in dimensionality from the (c) 3-D-perovskite (2.80 eV), to the (d) 2-D-Ruddlesden–Popper phase (1.36 eV).

dimensions has only a minor effect on the band gap. In the actual structure of Sr_2TiO_4, the axial bonds are slightly elongated (Ti–O_{ax} distance = 1.942 Å) in comparison to the equatorial bonds (Ti–O_{eq} distance = 1.915 Å) [24]. Calculations based on this structure show an increase of ~0.2 eV in the band gap, to a value of 2.01 eV.

The calculations show layered Ruddlesden–Popper compounds should not have significantly different band gaps from their 3-D ternary perovskite counterparts, provided the *M*–O bond distances and *M*–O–*M* bond angles are similar. The similarities between the 2-D and 3-D compounds should not have been unexpected since an earlier work by Wheeler et al. showed the electronic structure of three-dimensional d^n ReO_3 structures could be effectively modeled using two-dimensional structures [26]. As seen in Fig. 14 and Table 6, the calcium titanates have very similar band gaps for the $n = 2$, 3 and ∞ members of the Ruddlesden–Popper series, and the same can be said for $SrTiO_3$ and $Sr_3Ti_2O_7$. The only outlier in this series is Sr_2TiO_4, which has a band gap that is ~0.3 eV larger than $SrTiO_3$. The calculations suggest distortion of the TiO_6 octahedra accounts for ~0.2 eV of this increase. Thus, the change from the 3-D network of $SrTiO_3$ to the 2-D network of Sr_2TiO_4 causes only a very small perturbation of the band gap, consistent with the expectations from the band structure

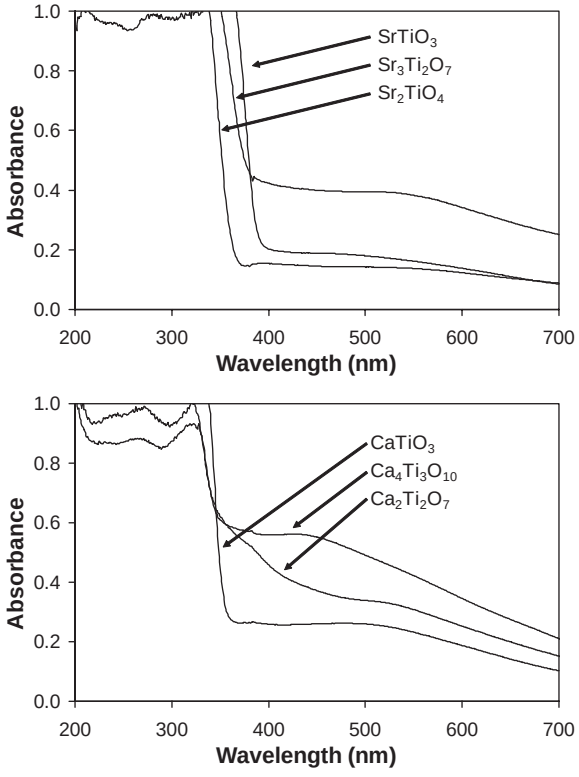

Fig. 14. Diffuse reflectance spectra for Ruddlesden–Popper compounds containing titanium.

Table 6
Measured and calculated band gaps for Ruddlesden–Popper phases

Compound	Measured E_g (eV)	Calculated E_g (eV)
$SrTiO_3$	3.1	2.02
Sr_2TiO_4	3.4	2.01
$Sr_3Ti_2O_7$	3.1	2.29
$CaTiO_3$	3.3	2.22
$Ca_3Ti_2O_7$	3.3	2.44
$Ca_4Ti_3O_{10}$	3.3	—

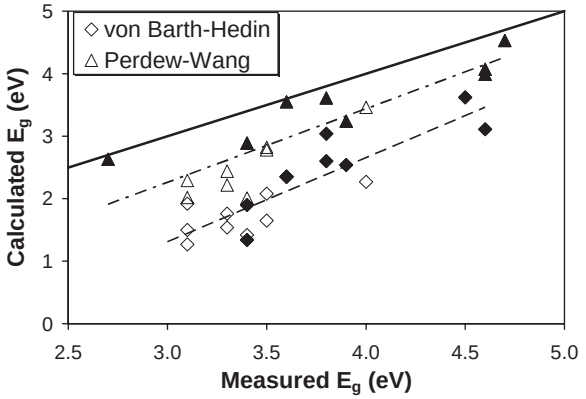

Fig. 15. LMTO calculated versus experimentally measured band gaps. The filled symbols represent ordered double perovskites. The solid black line shows the ideal 1-to-1 relationship between the calculated and measured band gaps. The upper and lower dot-dash lines show the linear fits to the band gaps obtained using the Perdew–Wang exchange (upper line, $E_g(\text{calc}) = 1.17\,E_g(\text{meas}) - 1.27$) and von Barth–Hedin exchange (lower line, $E_g(\text{calc}) = 1.34\,E_g(\text{meas}) - 2.72$).

calculations. Two final comments are in order regarding the diffuse reflectance spectra seen in Fig. 14. First of all, all compounds showed a non-zero baseline across the entire visible range. This baseline is likely a result of a very small degree of reduction, resulting in the creation of O^{2-} vacancies and free carriers that are known for many titanates. Secondly, for the $n = 2$ and 3 compounds the transition is less abrupt than for $SrTiO_3$, $CaTiO_3$ and Sr_2TiO_4. The origin of this difference is not certain, but it should be kept in mind that as *n* increases there is a corresponding increase in the variety of oxygen (bridging and terminal) and titanium environments. Such a change in crystal structure may lead to different transitions beginning at slightly different wavelengths, effectively spreading out the absorption edge.

4.5. Comparison of LMTO and experimental data

Plotting the calculated and measured band gaps together reveals an approximate linear correlation between the two (Fig. 15). Twenty-one compounds were

calculated using the von Barth–Hedin exchange correlation, and sixteen were calculated using the Perdew–Wang exchange correlation. Both exchange correlation approximations correctly predict the gross trends seen in the measured band gaps, but are less useful when it comes to predicting the absolute value. Using the von Barth–Hedin exchange, calculations for molybdenum compounds were problematic due to the lack of energetic mixing between molybdenum and other atomic orbitals. As discussed earlier the Perdew–Wang-based calculations were quite accurate for distorted ordered double perovskites, but underestimated the band gap once the electronically active octahedra were connected to each other. The implication is that the calculations overestimate the conduction band width. The band gaps of cubic ordered double perovskites were also underestimated. The exact origin of this effect is unknown. The linear relationships for both von Barth–Hedin and Perdew–Wang had similar confidence levels of 76.3% and 77.6%, respectively, but the linear fit parameters (ideally the slope would be 1 and the intercept 0) are considerably better for the Perdew–Wang exchange correlation.

5. Conclusions

Results show the band gaps of d^0 transition metal oxide perovskites depend upon the effective electronegativity of the transition metal ion, the connectivity of the octahedra, and the deviation from linearity of the M–O–M bonds. Changes in the identity and concentration of the electropositive spectator ions seem to have a minimal impact on the band gaps of these materials. In ordered double perovskites the band gap increases by $\sim$2 eV when the M-site cation was changed the metal ion with the highest effective electronegativity (Mo^{6+}) to the metal ion on the opposite end of our effective electronegativity scale (Ta^{5+}). Going from the isolated electronic structure of the ordered double perovskite to the three-dimensional connectivity of the ternary perovskite structure decreases the band gap by $\sim$0.8–1.5 eV, due to the increased width of the conduction band. Distorting the linear M–O–M bonds narrows the conduction band and can lead to an increase of as much as $\sim$0.5 eV in the band gap. Reducing the dimensionality of the structure from the 3-D connectivity of the ternary perovskite structure to the 2-D and pseudo 2-D connectivity of the layered perovskite phases (e.g., Ruddlesden–Popper phases) has a minimal direct impact on the band gap. However, dimensionality can have an impact if it triggers a change in the size and shape of the octahedra, as seen upon going from $SrTiO_3$ to Sr_2TiO_4. LMTO calculations give reasonably accurate predictions of the band gap values, when the Perdew–Wang exchange correlation is utilized in combination with O 2s and 2p valence orbitals. Even then the calculations appear to somewhat overestimate the conduction band width when the electronically active octahedra are connected, leading to an underestimation of the band gap. In general they are more useful for predicting trends than absolute values.

Acknowledgments

Thanks are due to O. Jepsen and O.K. Andersen at the Max Planck Institute (Stuttgart, Germany), C. Felser of Johannes Gutenberg University (Mainz, Germany), H. Kleinke of University of Waterloo (Waterloo, Canada) and R. Seshadri of University of California at Santa Barbara (USA). Professors Jepsen and Andersen provided the TB-LMTO-ASA version 47 code. Professor Felser's workshop at the 84th Canadian Society for Chemistry Conference introduced us to using LMTO calculations. Professor Kleinke assisted with the workshop. Professors Kleinke and Seshadri were both useful sources of information with regard to the LMTO calculations. Further thanks are due to M.W. Lufaso for providing the SPuDS program used in creating ideal perovskite structures. Financial support for this research was provided by the National Science Foundation, Grant No. DMR-0094271.

References

[1] A.J. Bard, Science 207 (1980) 139.
[2] A.J. Bard, M.A. Fox, Acc. Chem. Res. 28 (1995) 141.
[3] A. Fujishima, K. Honda, Nature 238 (1972) 37.
[4] O.K. Andersen, Phys. Rev. B 12 (1975) 3060.
[5] O.K. Andersen, O. Jepsen, Phys. Rev. Lett. 53 (1984) 2571.
[6] U. von Barth, L. Hedin, J. Phys. C 5 (1972) 1629.
[7] J.P. Perdew, Y. Wang, Phys. Rev. B 33 (1986) 8800.
[8] J. Ren, W. Liang, M.-H. Whangbo, Crystal and Electronic Structure Analysis Using CAESAR, 1998. The manual can be downloaded from http://www.PrimeC.com/.
[9] M.-H. Whangbo, R. Hoffmann, J. Am. Chem. Soc. 100 (1978) 6093.
[10] T.A. Albright, J.K. Burdett, M.-H. Whangbo, Orbital Interactions in Chemistry, Wiley, New York, 1985.
[11] P.M. Woodward, R.D. Hoffman, A.W. Sleight, J. Mater. Res. 8 (1994) 2118.
[12] L.H. Brixner, H.-Y. Chen, J. Electrochem. Soc. 130 (1983) 2435.
[13] C. Keller, Z. Anorg, Allgem. Chem. 318 (1962) 89.
[14] S.P. Tandon, J.P. Gupta, Phys. Stat. Sol. 38 (1970) 363.
[15] I.P. Shapiro, Opt. Spektrosk. 4 (1958) 256.
[16] E.A. Davis, N.F. Mott, Phil. Mag. 22 (1970) 903.
[17] L.F. Mattheiss, Phys. Rev. B 6 (1972) 4718.
[18] S. Saha, T.P. Sinha, A. Mookerjee, J. Phys.: Condens. Matter 12 (2000) 3325.
[19] M.W. Lufaso, P.M. Woodward, Acta. Crystallogr. B 57 (2001) 725.
[20] P.M. Woodward, J. Appl. Cryst. 30 (1997) 206.
[21] J.B. Goodenough, J. Appl. Phys. 81 (1997) 5330.
[22] S.N. Ruddlesden, P. Popper, Acta. Crystallogr. 11 (1958) 54.

[23] M.M. Elcombe, E. Kisi, K.D. Hawkings, T.J. White, P. Goodman, S. Matheson, Acta. Crystallogr. B 47 (1991) 305.
[24] K. Lukaszewicz, Rocz. Chem. 33 (1959) 239.
[25] G.M. Meyer, R.J. Nelmers, J. Hutton, Ferroelectrics 21 (1978) 461.
[26] R.A. Wheeler, M.-H. Whangbo, T. Hughbanks, R. Hoffmann, J.K. Burdett, T.A. Albright, J. Am. Chem. Soc. 108 (1986) 2222.
[27] H.J.A. Koopmanns, G.M.H. van de Velde, P.J. Gellings, Acta. Crystallogr. C 39 (1983) 1323.
[28] M.F. Kupriyanov, V.S. Filip'ev, Sov. Phys. Crystallogr. 8 (1963) 278.
[29] R. Zurmuhlen, E. Colla, D.C. Dube, J. Petzelt, I. Reaney, A. Bell, N. Setter, J. Appl. Phys. 76 (1994) 5864.
[30] S.M. Haile, B.J. Wuensch, E. Prince, Mater. Res. Soc. Symp. Proc. 166 (1990) 81.
[31] J.Y. Chan, I. Levin, T.A. Vanderah, R.G. Geyer, R.S. Roth, Int. J. Inorg. Mater. 2 (2000) 107.
[32] V.S. Filip'ev, E.G. Fesenko, Sov. Phys. Crystallogr. 10 (1966) 532.
[33] C.D. Brandle, V.J. Fratello, J. Mater. Res. 5 (1990) 2160.
[34] P. Balan, Trans. Indian Ceram. Soc. 60 (2001) 61.
[35] K. Henmi, Y. Hinatsu, N.M. Masaki, J. Solid State Chem. 148 (1999) 353.
[36] Y.J. Shan, A. Ozeki, W. Luan, T. Nakamura, M. Itoh, Ferroelectrics 264 (2001) 175.
[37] J.A. Noland, Phys. Rev. 94 (1954) 724.
[38] H. Mizoguchi, K. Ueda, M. Orita, S.-C. Moon, K. Kajihara, M. Hirano, H. Hosono, Mater. Res. Bull. 37 (2002) 2401.
[39] H. Kato, A. Kudo, J. Phys. Chem. B 104 (2001) 4285.